THE JOURNAL OF PHYSICAL CHEMISTRY C
A JOURNAL OF THE AMERICAN CHEMICAL SOCIETY

Defect-Assisted Photoemission in the hBN and TMDs/hBN Heterostructures

Yaolong Li,[⊥] Pengzuo Jiang,[⊥] Xiulan Liu,[⊥] Heng Wu, Xiaying Lyu, Xiaofang Li, Hai Lin, Jinglin Tang, Qinghong Lyu, Hong Yang, Chengyin Wu, Guowei Lu, Ping-Heng Tan, Liang-You Peng,[*] Yunan Gao,[*] Xiaoyong Hu,[*] and Qihuang Gong

Cite This: *J. Phys. Chem. C* 2024, 128, 4286−4294

Read Online

ACCESS | Metrics & More | Article Recommendations | Supporting Information

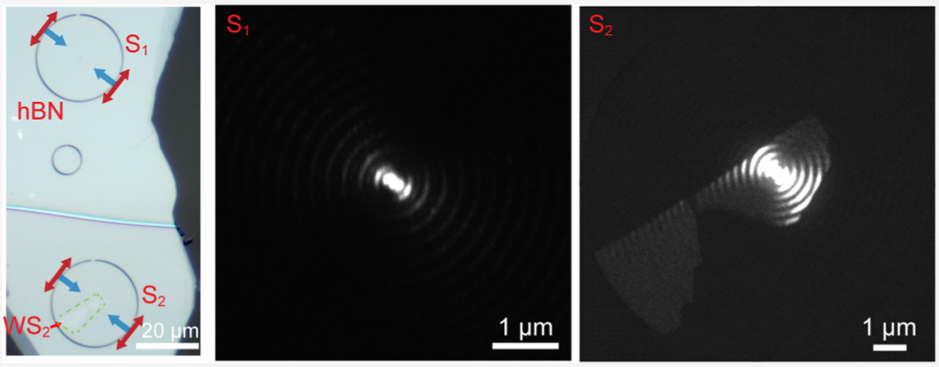

ABSTRACT: Ultrafast electron pulses have broad applications in the investigation of the ultrafast dynamics of materials and near-field nanophotonics. A hexagonal boron nitride (hBN) photoemission source has been proposed recently, characterized by a nanoscale working area and high brightness. However, the photoemission mechanisms of hBN are still not clear because the wide bandgap and low electron density of states of hBN are believed to result in low photoemission brightness. Here, we experimentally demonstrated the defect-assisted two-photon photoemission process in hBN by electron microscopy. The laser-induced defect states work as intermediate states to enhance the photoemission process by transferring a two-photon process to a cascaded one-photon process. In addition, we proposed another strategy to improve the photoemission brightness by increasing the density of states with a narrow-bandgap, two-dimensional material stacked on hBN. The photoemission intensity of the monolayer transition metal dichalcogenides (TMDs)/hBN heterostructure was largely enhanced, whereas the emission angle and energy spread remained similar to hBN. However, the photoemission intensity of TMDs/hBN can be influenced negatively by laser-induced defect trapping from the actual intermediate energy levels of TMDs. The defect-assisted photoemission process and heterostructure stacking strategy proposed here are instructive for the design of next-generation photoemission sources.

■ INTRODUCTION

Ultrafast electron pulses are vital components of ultrafast electron microscopy (UEM), photoinduced near-field electron microscopy (PINEM), and other ultrafast electron instruments,[1−4] possessing broad applications in the investigations of ultrafast dynamics of materials[5] and near-field nanophotonics,[6] etc. The ultrafast electron pulses are usually generated by photoemission sources driven by femtosecond laser, including sharp-tip photocathodes and flat photocathodes.[7−13] The two types of photocathodes have different advantages, concerning the size of the working area, emission angle, energy spread, and intensity. For example, sharp tip photocathodes generally have a much smaller working area compared to flat photocathodes, while the latter exhibit a smaller emission angle. Both of these factors contribute to the enhancement of electron-coherent features.[7,8] Therefore, the simultaneous realization of the small working area and emission angle to enhance electron coherence will be desirable.[14] Many photocathode materials have been proposed, such as W(ZrO), LaB_6, carbon nanotubes, and semiconductor or dielectric materials.[8,13,15−17] Recently, we proposed a new material for a photoemission source, hexagonal boron nitride (hBN), possessing both nanoscale bright intensity and a near-vertical photoemission angle by using a designed nanostructure under a ~400 nm femtosecond laser.[18] The hBN is a van der Waals material with

Received: November 29, 2023
Revised: January 31, 2024
Accepted: February 16, 2024
Published: February 28, 2024

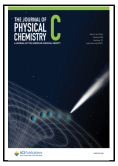

a wide bandgap (~6 eV) and a high refractive index (in-plane $n > 2.1$) from ultraviolet to near-infrared.[19−21] Nanoscale light localization can be realized with hBN planar waveguide modes excited from an etch ring slit under an ~400 nm femtosecond laser. However, the photoemission mechanisms of hBN are still not clear because the wide bandgap and low electron density of states (DOSs) of hBN are believed to result in low photoemission brightness, which are inconsistent with the experimental observations.

The photoemission process of hBN is regarded as a two-photon process when excited with ~400 nm laser, i.e., $P_E = \alpha I^2$, where P_E is the photoemission intensity, I is the local field intensity, and α is the photoemission efficiency. The local field intensity of hBN can be largely enhanced on the nanoscale by the designed structures. However, the photoemission efficiency of hBN material is regarded as quite low due to the wide bandgap and low electron density of states (DOSs), which should limit the photoemission intensity. Up to now, the underlying physics of the photoemission process of the hBN emitter is still not well understood and should be investigated in the following step. In addition, to further improve the photoemission brightness of hBN-based emitters, an alternative strategy is to increase the DOSs with a narrow-bandgap two-dimensional (2D) material stacked on hBN, such as graphene and monolayer transition metal dichalcogenides (TMDs).[22−24]

In this work, we revealed the defect-assisted two-photon photoemission process in hBN by photoemission electron microscopy (PEEM). The defect states were introduced during laser illumination and located at the nanoscale focusing spot at the hBN surface. The defect states serve as intermediate states in the wide bandgap of hBN, transferring a two-photon process to a cascaded one-photon process and largely improving the photoemission efficiency. In addition, we proposed another strategy to improve the photoemission brightness by increasing the density of states with narrow-bandgap two-dimensional TMDs stacked on hBN. The photoemission intensities of the monolayer TMDs/hBN heterostructures, such as WS_2/hBN and $MoSe_2$/hBN, were largely enhanced, whereas the emission angle and energy spread remained similar to hBN. However, the photoemission intensity of TMDs/hBN can be influenced negatively by defect trapping from the actual intermediate energy levels of TMDs. It should be noted that although more stable monolayer materials with large DOSs should be explored further for practical applications, the heterostructure stacking strategies proposed here are instructive for the design of next-generation photoemission sources. In addition, the laser-induced defects in hBN found in this work are potentially controllable and can be a platform for the investigations of electron−phonon interactions, single-photon emitters, and quantum optics in hBN in the future.[25,26]

■ METHODS

Sample Fabrication and Characterizations. The hBN flakes were mechanically exfoliated on polydimethylpolysiloxane (PDMS) sheets from bulk crystals (2D Semiconductors), and the thicknesses of the hBN flakes were estimated by the reflected color under optical microscopy. Then, the selected hBN flakes were transferred to the soda-lime glass substrate with an ~10 nm indium tin oxide (ITO) layer by using the all-dry transfer method under optical microscopy. Monolayer TMDs (WS_2 and $MoSe_2$) were also exfoliated and transferred onto the hBN flakes. Then the transferred hBN flakes with monolayer TMDs were etched with a series of nanostructures by using a focused ion beam (FIB) to support the desired near-field modes. All samples were annealed under an ultrahigh vacuum (approximately 10^{-9} Torr) at 200 °C for 2 h before loading into the PEEM chamber. After PEEM experiments, the samples were characterized with atomic force microscopy (AFM), scanning electron microscopy (SEM), photoluminescence (PL), and Raman spectra. The PL and Raman spectra were collected by an inverted microscope (Eclipse Ti-2 inverted microscope, Nikon) with an objective lens (100×, NA = 0.9) and measured by a spectrometer (Kymera 328i, Andor). The excitation source was a continuous 442 nm laser at 0.1 mW. A 150 lines/mm grating was used for PL spectra, and an 1800 lines/mm grating was used for Raman spectra. In addition, the Raman spectra for WS_2 were measured using a Jobin-Yvon HR800 micro-Raman system with an 1800 lines/mm grating and a continuous 532 nm laser.

PEEM Measurements. The PEEM measurements were performed by using a high-resolution low-energy electron microscopy (LEEM)/PEEM system (ACSPELEEM III, Elmitec GmbH) equipped with a hemispherical electron energy analyzer. This PEEM system can support real-space, momentum-space, and energy-space measurements. The energy-resolved PEEM measurements were performed in the imaging mode by inserting a 12.5 μm energy slit and sweeping the start voltage in a step of 0.1 eV to allow electrons with different energies to pass through the energy slit. A commercial Ti:sapphire femtosecond laser (Mai Tai HP, Spectra-Physics, pulse duration: 80−100 fs) operated at 690−1040 nm (2.9 W @ 820 nm) with a repetition rate of 80 MHz was used as the laser source to pump an optical parametric oscillator (OPO) (Inspire Auto 100, Spectra-Physics). The second harmonic generation (SHG) port (390−440 nm, 1.0 W @ 410 nm) was used to provide an excitation laser for the static PEEM measurements. The pulses were focused on the sample surface at normal incidence, with a spot diameter of approximately 150 μm. The polarization of the laser is adjusted through a 1/4 waveplate or a 1/2 waveplate.

First-Principle Calculations. The band structures and DOSs were calculated within the framework of density functional theory using the Vienna ab initio simulation package (VASP). The interaction between nuclei and core electrons was represented by a projector augmented wave pseudopotential. The Perdew−Burke−Ernzerhof (PBE) exchange−correlation function within the generalized gradient approximation was used to describe the complex interactions between valence electrons. The monolayer hBN has a hexagonal honeycomb structure with a lattice constant of 2.512 Å. A vacuum layer of 15 Å along the z-axis was applied to eliminate the interactions between periodic images. The lattice constants of WS_2 are $a = 3.153$ Å and $c = 12.323$ Å. During the self-consistent and band structure calculations, the cutoff energy for the plane wave basis was 500 eV, and the Brillouin zone was sampled with the $39 \times 39 \times 1$ Monhkorst-Pack type k-point grid. In order to investigate the influence of light-induced defects, $3 \times 3 \times 1$ hBN and WS_2 supercells were built. Based on the pristine supercell, a B atom was deleted to get the B vacancy in the hBN system, while a N atom was absent in the N vacancy system. For WS_2, a S atom was deleted to create a S vacancy. Before electronic structure calculations, the geometries of these defective systems were fully relaxed until the Hellmann−Feynman force was less than 0.01 eV/Å. Due to the large number of atoms, a $9 \times 9 \times 1$ k-point mesh was

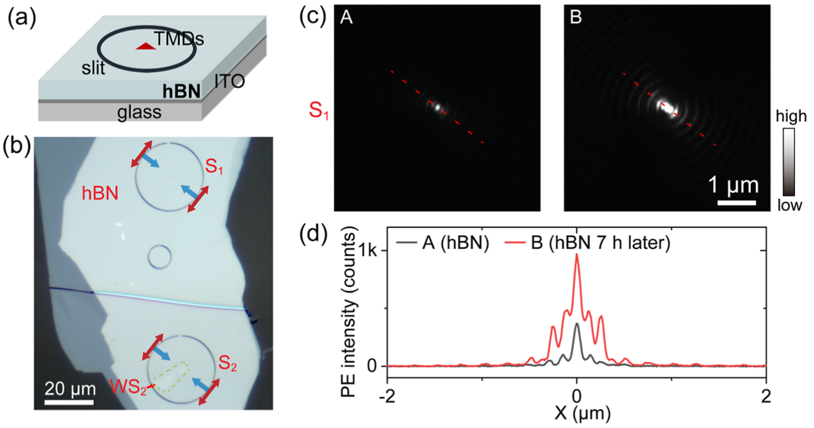

Figure 1. Structure and characterization of the hBN photoemission emitter. (a) Schematic of the sample structures for hBN and monolayer TMDs/hBN fabricated with focused ion beams (FIB). (b) Optical image of a representative sample. S$_1$ and S$_2$ are hBN and WS$_2$/hBN structures, respectively. (c) PEEM image for S$_1$ measured with a 415 nm laser with linear polarization (red arrow in b) at normal incidence. The TE mode of hBN waveguide was excited from the ring slit and focused toward the ring center (along the blue arrow in b). The brightness of the image in (c) is adjusted to be oversaturated for better viewing. The PEEM image B in (c) was measured several hours later than A, and the corresponding crosscut lines are shown in (d).

used in the subsequent self-consistency and band calculations. The user-friendly postprocessing package VASPKIT was used to treat the band unfolding calculations.

RESULTS AND DISCUSSION

The sample was fabricated by mechanical exfoliation and dry transfer of hBN onto a glass substrate with an ~10 nm ITO layer and following etching of nanostructures with focused ion beams (FIB), as shown in Figure 1a. Because hBN has a wide bandgap and high refractive index, the vacuum/hBN/glass structure can support planar waveguide mode in the visible range. Herein, the thickness of hBN was chosen between 60−80 nm to support the fundamental TE mode for the excitation wavelengths of 400−450 nm. The ~10 nm ITO was used to avoid the surface charging effect during photoemission. The ring slit etched by FIB worked as the coupler to couple the planar laser beam from normal incidence into the waveguide mode and form a nanoscale focusing in the center of ring. The representative optical image of experimental sample is shown in Figure 1b with etched rings on 60 nm hBN. The radius for hBN structure S$_1$ was set as 13.8 μm (60 × λ_{eff}) and the slit width was 170 nm. Here, λ_{eff} = 230 nm is the effective wavelength of the waveguide mode for an excitation wavelength of around 410 nm. The hBN structure S$_1$ can support nanofocusing mode when excited with 415 nm laser with linear polarization at normal incidence, which can be well imaged with PEEM. As shown in Figure 1c (left part), a strong focusing spot in the center of hBN structure S$_1$ can be clearly observed in the PEEM image. We also noticed the intensity of the focusing spot increased after laser illumination for several hours (shown in Figure 1c, from A to B), and the cross-cut lines are plotted in Figure 1d for better comparison. The increase of photoemission intensity under laser illumination indicates the change of material properties at the focusing spot that enhances the DOSs and photoemission efficiency. The underlying mechanism of the enhancement of photoemission efficiency will be discussed later.

To further improve the photoemission brightness by increasing the DOSs, another strategy is to stack a 2D material with a narrow-bandgap on hBN, such as monolayer TMDs. As shown in Figure 1b, the WS$_2$/hBN heterostructure S$_2$ was fabricated with the same size as S$_1$. The monolayer WS$_2$ was transferred to the substrate before FIB etching to ensure the WS$_2$ flake was precisely located at the focusing spot, as shown in the PEEM image (Figure 2a). The monolayer WS$_2$ is outlined in Figure 2b, with a lateral size of ~2 μm across the red dashed line. The photoemission intensity from WS$_2$ is obviously higher than that from the surrounding hBN in Figure 2b. Especially, the bright interference fringes can be observed only on WS$_2$, indicating that the photoemission efficiency of WS$_2$ is much higher than that of hBN. To compare photoemission intensities of hBN and WS$_2$/hBN structures, we measured the photoemission intensities at the identical laser powers (Figure 2c). A strong nanofocusing spot was observed for WS$_2$/hBN with a size of ~70 nm, and the

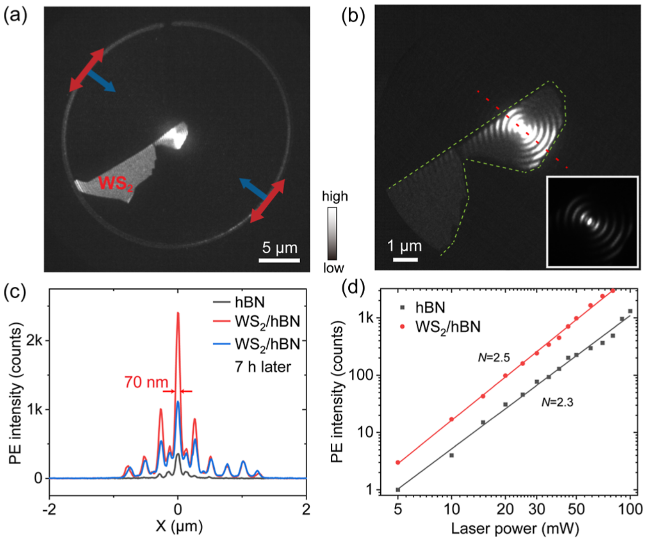

Figure 2. Photoemission intensities for the hBN and WS$_2$/hBN structures. (a,b) PEEM images for the WS$_2$/hBN structure excited with a 415 nm laser of 70 mW, with linear polarization (red arrow) at normal incidence. (c) Photoemission intensities for the hBN and WS$_2$/hBN structures along the crosscut line in (b). (d) Power-dependent photoemission intensities for the two structures; N denotes the nonlinear order of photoemission.

photoemission intensity was enhanced ∼7 times compared with the hBN structure. The power-dependent photoemission intensities are shown in Figure 2d, indicating a two-photon process, and the photoemission enhancement for WS_2/hBN was kept in a broad power range. It should be noted that similar results were also observed for the monolayer $MoSe_2$/hBN heterostructure, with a ∼60 nm nanofocusing and ∼12 times enhancement (see Section 2 of the Supporting Information). We also observed a decrease of photoemission intensity of TMDs/hBN after laser illumination for several hours (Figure 2c) differently from that of hBN, which indicates a decrease of the DOSs and photoemission efficiency.

The photoemission intensity depends on both the local field intensity and the photoemission efficiency. The influence of monolayer TMDs on the nanofocusing local field intensity of hBN waveguide should be considered because TMDs have a considerable optical absorption even at the monolayer. As shown in Figure 3a, for the WS_2/hBN structure excited from a line slit with 415 nm laser, the severe damping of waveguide mode during propagation is clearly observed in the nanophotonic simulations with the finite-difference time-domain method, whereas the mode supported by hBN alone has little decay. Specifically, the field intensity $|E|^2$ has a 50% decrease within 1.6 μm and 90% decrease within 5.4 μm for the WS_2/hBN structure, which indicates that smaller sizes for WS_2 are preferable, and the optimal size is just limited to cover the central 100 nm focusing spot. To show the influence of WS_2 absorption more directly, the focusing intensity of the hBN ring slit (radius of 6.9 μm) with a monolayer WS_2 disk in the center was simulated, as shown in Figure 3b. The focusing pattern in Figure 3b is consistent with the PEEM experiment, and the focusing intensity is 44% decreased for WS_2 with a radius of 1 μm. In Figure 2b, the size of WS_2 from the center to edge along the red dashed line is ∼1 μm; thus, the field intensity is evaluated to have a half decrease from the simulations. Considering the experimental ∼7 times photoemission enhancement in Figure 2 and the decreased local field intensity, the photoemission efficiency of WS_2/hBN is evaluated to be 20 times higher than hBN. The heavy influence of TMDs' absorption can also be observed by changing the polarization of excitation laser to allow waveguide mode passing through different lengths of monolayer TMDs, as shown in Figure 3c. In addition, the larger photoemission enhancement for the $MoSe_2$/hBN structure discussed above could be due to the smaller size of monolayer $MoSe_2$ compared with WS_2.

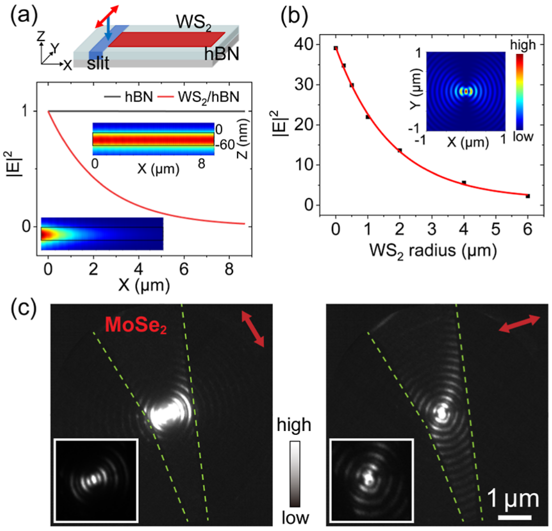

Figure 3. Local field intensity damping by the absorption of monolayer TMDs. (a) Simulated field intensity damping of the waveguide mode for hBN and WS_2/hBN structures excited from a line slit. The corresponding electric field intensity profiles along the propagation direction (X–Z plane) are shown as insets. (b) Simulated focusing intensity of the hBN ring slit (radius of 6.9 μm) with a monolayer WS_2 disk of different radiuses in the center. (c) PEEM images to show the influence of monolayer TMDs' absorption on the focusing intensity by changing the polarization of the excitation laser to allow waveguide mode passing through different lengths of monolayer $MoSe_2$.

The photoemission mechanisms for hBN and TMDs/hBN are discussed as follows. The photoemission efficiency is mainly determined by the DOSs and work function for two-photon processes. Since the work functions are similar for hBN and TMDs,[27−29] the main influence on photoemission efficiency stems from DOSs. In Figure 4a–d, for pristine hBN and WS_2, we show the theoretical calculation results for band structures along Γ-K and the DOSs around the Γ point. As shown in Figure 4a, the two-photon process for pristine hBN has no actual intermediate states involved in the wide bandgap. It indicates that simultaneous absorption of two photons is necessary for the photoemission process and results in low photoemission efficiency, consistent with the experimental observation for initial hBN. In contrast, for pristine monolayer TMDs, the photoemission process can be assisted by the actual intermediate states in the conduction band of TMDs, which largely enhance the photoemission efficiency. Therefore, strong photoemission intensities were observed for the initial TMDs/hBN structures. The difference in band structures and DOSs can account for the photoemission intensities of the initial hBN and TMDs/hBN structures. It should be noted that the DOSs around the Γ point are emphasized here because of the small photoemission horizon set by the limited photon energies.

Considering the band structures of hBN and TMDs, we attribute the laser illumination effect to laser-induced defect states because defects can be efficiently introduced by laser illumination for low-dimensional materials. For hBN, B and N vacancy defects have been reported by many groups and can work as single-photon emitters.[25,30−33] These defect states can create new interband energy levels in the wide bandgap of hBN.[32,34−36] For TMDs, monolayer TMDs can easily accumulate defects such as S vacancy under laser illumination, as recently reported.[37−41] The defect states in the bandgap can trap photoexcited electrons from conduction bands of TMDs.[25,39,41−43] For the photoemission process of defective hBN, the interband defect states can work as intermediate states to convert the two-photon process to the cascaded one-photon process and largely improve the photoemission efficiency. For the photoemission process of defective TMDs, the case is different because there are already actual intermediate energy levels in the conduction bands. The lifetimes of electrons in the intermediate energy levels play an important role in the final photoemission intensity. The defect states in the bandgap can trap electrons in the conduction bands. The defect trapping process has been reported to be quite fast and reduces the electron lifetime in the intermediate energy levels.[39,43,44] Therefore, the photoemission intensity should be lowered by laser-induced defect states for the

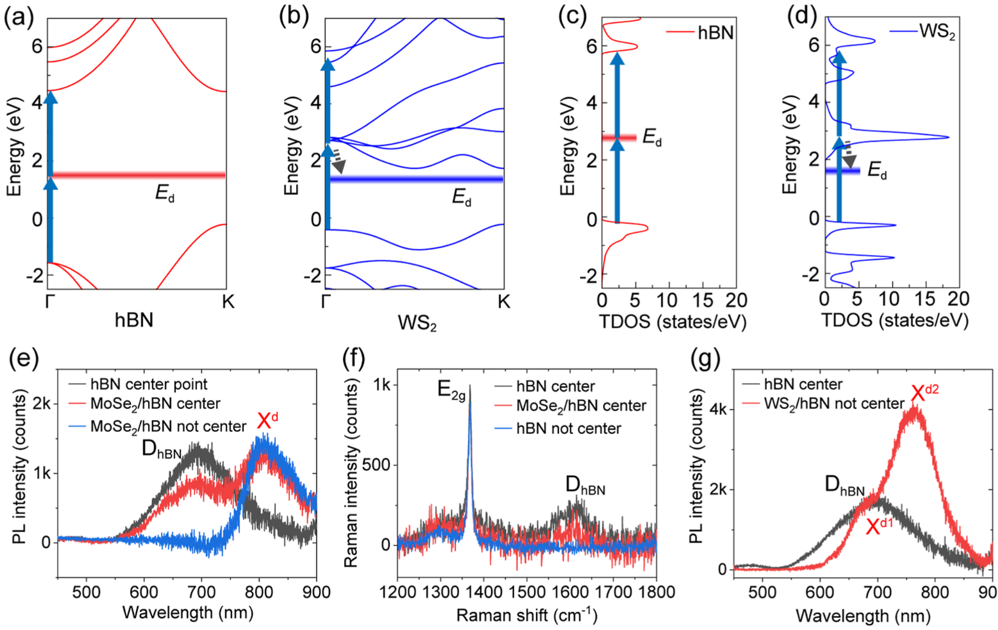

Figure 4. Photoemission processes of hBN and monolayer TMDs and the effect of laser-induced defect states. (a−d) Band structures and total DOSs of pristine hBN and monolayer WS_2. Two-photon photoemission processes for hBN and WS_2 are also plotted as blue arrows. E_d denotes laser-induced defect states. The energy axis in (c,d) is shifted for better comparison. (e−g) Defect signatures from photoluminescence and Raman spectra for hBN and monolayer TMDs measured at room temperature. D_{hBN} denotes the defect peak of hBN, X^d denotes the defect-bonded exciton peak of $MoSe_2$, and X^{d1} and X^{d2} denote the defect-bonded exciton peaks of WS_2.

TMDs/hBN heterostructure. The different roles of defect states for hBN and TMDs result in opposite effects on photoemission intensity. It should be noted that although more stable monolayer materials should be explored further for practical applications, the heterostructure stacking strategies proposed here are still instructive for the design of next-generation photoemission sources. To efficiently enhance the photoemission of hBN, other methods such as element doping or alkali metal evaporation could also be possible by increasing the DOSs or lowering the work function.

The electronic properties at the heterostructure interface formed by monolayer TMDs and bulk hBN should be discussed because the interfacial properties can have implications for charge transfer dynamics, local DOSs, and overall photoemission characteristics. For the pristine TMDs/hBN heterostructure, the influence of interfacial properties could be less important because the bandgap of hBN is much larger than that of monolayer TMDs, and the hBN is generally regarded as a dielectric environment for the monolayer TMDs. For defective hBN, the midgap defect states in hBN provide extra local DOS. There could be charge transfer between the conduction bands of monolayer TMDs and the defect states of hBN. It should be noted that the photoemission process is quite surface sensitive, which means the photoemitted electrons are mostly from the top monolayer TMDs, rather than from the underlying hBN. The defect states in hBN could also possibly trap electrons from the conduction bands of monolayer TMDs, as the defect states in TMDs can lower the photoemission intensity. In addition, because the defects are introduced by laser illumination, it can be predicted that there should be further defect accumulation under prolonged laser exposure, which could lead to the degradation of photoemission performance over time for both hBN and TMDs.

The presence of defect states can be evidenced by the PL and Raman spectra, as shown in Figure 4e−g. A broad PL peak centered at 700 nm is observed for hBN measured in the ring center (Figure 4e), which could be attributed to defect states of mixed B and N vacancies.[25,32,33,45] Importantly, the PL feature can only be observed in the ring center (focusing spot), which is strong evidence of laser-induced defects. Besides, the presence of defect states for hBN can also be observed in Raman spectra (Figure 4e), where defect peaks ∼1610 cm^{-1} can be identified, consistent with reports.[46] For monolayer TMDs, defect-bonded exciton peaks can be observed in the PL spectra (Figure 4e), whereas the original exciton peaks are strongly quenched by defect states. It should be noted that the defect signals were observed in the entire monolayer TMDs, probably because the monolayer material can easily accumulate defects. In addition, we also observed the signatures of defect states for TMDs/hBN structures from PEEM images excited with a 273 nm ultraviolet (UV) laser (see Section 4 of the Supporting Information). Nevertheless, one cannot directly observe the defect sites in PEEM experiments because the atomic sizes of defects are out of the 10s nm spatial resolution of PEEM, and the defect types and densities are hard to evaluate. The calculated DOSs for defective hBN and WS_2 are shown in Section 6 of the Supporting Information. It should be noted that the defect states in hBN have drawn much attention in many fields due to the rich underlying physics and potential applications in quantum information and sensing. The method of introducing defect states in hBN with laser excitation reported here is potentially controllable to produce nanoscale defects at specific sites. The controllable laser-induced defects in hBN can be a platform for the investigations of electron−phonon interactions, single-photon emitters, and quantum optics in the future.[25,26]

Apart from the photoemission intensity, the emission direction and energy spread of a photoemission source are also important and should be discussed, which can be measured with PEEM in momentum and energy spaces. The photoemission properties in momentum and energy spaces for hBN and $MoSe_2$/hBN structures are depicted in Figure 5a,b.

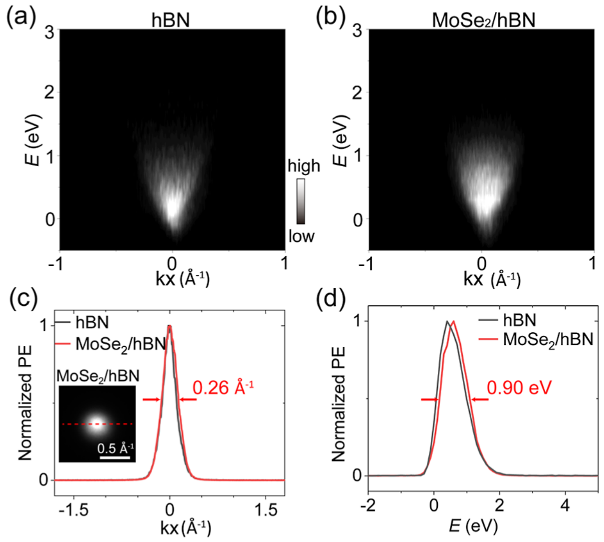

Figure 5. Photoemission properties in momentum and energy spaces for hBN and TMDs/hBN structures. (a,b) Photoemission intensity vs momentum and energy for hBN and $MoSe_2$/hBN structures, respectively. (c) Energy-integrated photoemission intensities in the momentum space for the two structures (along the dashed red line in the inset). (d) Momentum-integrated electronic energy distribution curves for the two structures.

The photoemission intensities present a localized distribution in the energy domain around the Γ-point for both structures. The energy-integrated photoemission intensities in the momentum space are nearly overlapped for the two structures (Figure 5c), attributed to the flat surface of both structures. In addition, the momentum-integrated electronic energy distribution curves are also nearly overlapped for hBN and $MoSe_2$/hBN (Figure 5d). For WS_2/hBN, similar results were observed, except that there is an energy shift between WS_2/hBN and hBN (see Section 3 of the Supporting Information), possibly due to the lower valence band position of WS_2 compared with that of $MoSe_2$.[27−29] Therefore, the differences in photoemission properties in momentum and energy spaces are insignificant between hBN and the TMDs/hBN structures.

■ CONCLUSIONS

In summary, we revealed the defect-assisted two-photon photoemission process in hBN by photoemission photoelectron microscopy (PEEM). The defect states were introduced during laser illumination and located at the nanoscale focusing spot at the hBN surface. The defect states work as intermediate states in the wide bandgap of hBN for the photoemission process, transferring two-photon to the cascaded one-photon process and largely improving the photoemission intensity. In addition, the photoemission brightness can be further improved by increasing the density of states with narrow-bandgap two-dimensional TMDs stacked on hBN. The photoemission intensities of the monolayer TMDs/hBN heterostructures, such as WS_2/hBN and $MoSe_2$/hBN, were largely enhanced, whereas the emission angle and energy spread remained similar to hBN. However, the photoemission intensity of TMDs/hBN can be influenced negatively by laser-induced defect trapping from the actual intermediate energy levels of TMDs. The effects of defect states were also analyzed by band structure and DOS calculations, and the presence of defect states was verified by PL and Raman spectra. The photoemission mechanism and heterostructure stacking strategies proposed here are instructive for the design of next-generation photoemission sources. In addition, the laser-induced defects in hBN found in this work are potentially controllable and can be a platform for the investigations of electron−phonon interactions, single-photon emitters, and quantum optics in hBN in the future.

■ ASSOCIATED CONTENT

SI Supporting Information

The Supporting Information is available free of charge at https://pubs.acs.org/doi/10.1021/acs.jpcc.3c07843.

> SEM images of the hBN structure; PEEM measurements for the $MoSe_2$/hBN structure; photoemission properties in momentum and energy spaces for the WS_2/hBN structure; PEEM imaging of defects with UV laser; photoemission patterns under different excitation wavelengths; band structures and total DOSs of defective systems; and cutoff thickness for the waveguide mode (PDF)

■ AUTHOR INFORMATION

Corresponding Authors

Liang-You Peng − *State Key Laboratory for Mesoscopic Physics & Department of Physics, Collaborative Innovation Center of Quantum Matter and Frontiers Science Center for Nano-optoelectronics, Beijing Academy of Quantum Information Sciences, Peking University, Beijing 100871, China; Peking University Yangtze Delta Institute of Optoelectronics, Nantong 226010 Jiangsu, China; Collaborative Innovation Center of Extreme Optics, Shanxi University, Taiyuan 030006 Shanxi, China;* Email: liangyou.peng@pku.edu.cn

Yunan Gao − *State Key Laboratory for Mesoscopic Physics & Department of Physics, Collaborative Innovation Center of Quantum Matter and Frontiers Science Center for Nano-optoelectronics, Beijing Academy of Quantum Information Sciences, Peking University, Beijing 100871, China; Peking University Yangtze Delta Institute of Optoelectronics, Nantong 226010 Jiangsu, China; Collaborative Innovation Center of Extreme Optics, Shanxi University, Taiyuan 030006 Shanxi, China;* orcid.org/0000-0002-3131-7559; Email: gyn@pku.edu.cn

Xiaoyong Hu − *State Key Laboratory for Mesoscopic Physics & Department of Physics, Collaborative Innovation Center of Quantum Matter and Frontiers Science Center for Nano-optoelectronics, Beijing Academy of Quantum Information Sciences, Peking University, Beijing 100871, China; Peking University Yangtze Delta Institute of Optoelectronics, Nantong 226010 Jiangsu, China; Collaborative Innovation Center of Extreme Optics, Shanxi University, Taiyuan 030006 Shanxi, China;* orcid.org/0000-0002-1545-1491; Email: xiaoyonghu@pku.edu.cn

Authors

Yaolong Li − *State Key Laboratory for Mesoscopic Physics & Department of Physics, Collaborative Innovation Center of Quantum Matter and Frontiers Science Center for Nano-optoelectronics, Beijing Academy of Quantum Information*

Sciences, Peking University, Beijing 100871, China; orcid.org/0000-0002-1457-190X

Pengzuo Jiang − *State Key Laboratory for Mesoscopic Physics & Department of Physics, Collaborative Innovation Center of Quantum Matter and Frontiers Science Center for Nano-optoelectronics, Beijing Academy of Quantum Information Sciences, Peking University, Beijing 100871, China*

Xiulan Liu − *State Key Laboratory for Mesoscopic Physics & Department of Physics, Collaborative Innovation Center of Quantum Matter and Frontiers Science Center for Nano-optoelectronics, Beijing Academy of Quantum Information Sciences, Peking University, Beijing 100871, China*

Heng Wu − *State Key Laboratory of Superlattices and Microstructures, Institute of Semiconductors, Chinese Academy of Sciences, Beijing 100083, China*

Xiaying Lyu − *State Key Laboratory for Mesoscopic Physics & Department of Physics, Collaborative Innovation Center of Quantum Matter and Frontiers Science Center for Nano-optoelectronics, Beijing Academy of Quantum Information Sciences, Peking University, Beijing 100871, China*

Xiaofang Li − *State Key Laboratory for Mesoscopic Physics & Department of Physics, Collaborative Innovation Center of Quantum Matter and Frontiers Science Center for Nano-optoelectronics, Beijing Academy of Quantum Information Sciences, Peking University, Beijing 100871, China*

Hai Lin − *State Key Laboratory for Mesoscopic Physics & Department of Physics, Collaborative Innovation Center of Quantum Matter and Frontiers Science Center for Nano-optoelectronics, Beijing Academy of Quantum Information Sciences, Peking University, Beijing 100871, China*

Jinglin Tang − *State Key Laboratory for Mesoscopic Physics & Department of Physics, Collaborative Innovation Center of Quantum Matter and Frontiers Science Center for Nano-optoelectronics, Beijing Academy of Quantum Information Sciences, Peking University, Beijing 100871, China*

Qinghong Lyu − *State Key Laboratory for Mesoscopic Physics & Department of Physics, Collaborative Innovation Center of Quantum Matter and Frontiers Science Center for Nano-optoelectronics, Beijing Academy of Quantum Information Sciences, Peking University, Beijing 100871, China*

Hong Yang − *State Key Laboratory for Mesoscopic Physics & Department of Physics, Collaborative Innovation Center of Quantum Matter and Frontiers Science Center for Nano-optoelectronics, Beijing Academy of Quantum Information Sciences, Peking University, Beijing 100871, China; Peking University Yangtze Delta Institute of Optoelectronics, Nantong 226010 Jiangsu, China; Collaborative Innovation Center of Extreme Optics, Shanxi University, Taiyuan 030006 Shanxi, China*

Chengyin Wu − *State Key Laboratory for Mesoscopic Physics & Department of Physics, Collaborative Innovation Center of Quantum Matter and Frontiers Science Center for Nano-optoelectronics, Beijing Academy of Quantum Information Sciences, Peking University, Beijing 100871, China; Peking University Yangtze Delta Institute of Optoelectronics, Nantong 226010 Jiangsu, China; Collaborative Innovation Center of Extreme Optics, Shanxi University, Taiyuan 030006 Shanxi, China;* orcid.org/0000-0001-5733-6427

Guowei Lu − *State Key Laboratory for Mesoscopic Physics & Department of Physics, Collaborative Innovation Center of Quantum Matter and Frontiers Science Center for Nano-optoelectronics, Beijing Academy of Quantum Information Sciences, Peking University, Beijing 100871, China; Peking University Yangtze Delta Institute of Optoelectronics, Nantong 226010 Jiangsu, China; Collaborative Innovation Center of Extreme Optics, Shanxi University, Taiyuan 030006 Shanxi, China;* orcid.org/0000-0003-0646-6971

Ping-Heng Tan − *State Key Laboratory of Superlattices and Microstructures, Institute of Semiconductors, Chinese Academy of Sciences, Beijing 100083, China;* orcid.org/0000-0001-6575-1516

Qihuang Gong − *State Key Laboratory for Mesoscopic Physics & Department of Physics, Collaborative Innovation Center of Quantum Matter and Frontiers Science Center for Nano-optoelectronics, Beijing Academy of Quantum Information Sciences, Peking University, Beijing 100871, China; Peking University Yangtze Delta Institute of Optoelectronics, Nantong 226010 Jiangsu, China; Collaborative Innovation Center of Extreme Optics, Shanxi University, Taiyuan 030006 Shanxi, China*

Complete contact information is available at:
https://pubs.acs.org/10.1021/acs.jpcc.3c07843

Author Contributions

$^{\perp}$Y.L., P.J. and X.L. contributed equally to this work.

Notes

The authors declare no competing financial interest.

■ ACKNOWLEDGMENTS

This work was supported by the following grants: the National Key Research and Development Program of China (grant nos. 2018YFB2200403, 2018YFA0704404, and 2018YFA0306302), the National Natural Science Foundation of China (grant nos. 91950204, 92150302, 92250303, 92250305, 61875002, 12174011, and 12234002), the Guangdong Major Project of Basic and Applied Basic Research (grant no. 2020B0301030009), the Innovation Program for Quantum Science and Technology (grant no. 2021ZD0301500), and the National Postdoctoral Program for Innovative Talents (grant no. 8206200074).

■ REFERENCES

(1) Vanacore, G. M.; Fitzpatrick, A. W. P.; Zewail, A. H. Four-dimensional electron microscopy: Ultrafast imaging, diffraction and spectroscopy in materials science and biology. *Nano Today* **2016**, *11* (2), 228−249.

(2) Sciaini, G.; Miller, R. J. D. Femtosecond electron diffraction: heralding the era of atomically resolved dynamics. *Rep. Prog. Phys.* **2011**, *74* (9), 096101.

(3) Barwick, B.; Flannigan, D. J.; Zewail, A. H. Photon-induced near-field electron microscopy. *Nature* **2009**, *462* (7275), 902−906.

(4) Polman, A.; Kociak, M.; García de Abajo, F. J. Electron-beam spectroscopy for nanophotonics. *Nat. Mater.* **2019**, *18* (11), 1158−1171.

(5) Liao, B.; Zhao, H.; Najafi, E.; Yan, X.; Tian, H.; Tice, J.; Minnich, A. J.; Wang, H.; Zewail, A. H. Spatial-Temporal Imaging of Anisotropic Photocarrier Dynamics in Black Phosphorus. *Nano Lett.* **2017**, *17* (6), 3675−3680.

(6) Kurman, Y.; Dahan, R.; Sheinfux, H. H.; Wang, K.; Yannai, M.; Adiv, Y.; Reinhardt, O.; Tizei, L. H. G.; Woo, S. Y.; Li, J.; et al. Spatiotemporal imaging of 2D polariton wave packet dynamics using free electrons. *Science* **2021**, *372* (6547), 1181−1186.

(7) Zhang, L.; Hoogenboom, J. P.; Cook, B.; Kruit, P. Photoemission sources and beam blankers for ultrafast electron microscopy. *Struct. Dyn.* **2019**, *6* (5), 051501.

(8) Zhou, S.; Chen, K.; Cole, M. T.; Li, Z.; Chen, J.; Li, C.; Dai, Q. Ultrafast Field-Emission Electron Sources Based on Nanomaterials. *Adv. Mater.* **2019**, *31* (45), 1805845.

(9) Schenk, M.; Krüger, M.; Hommelhoff, P. Strong-Field Above-Threshold Photoemission from Sharp Metal Tips. *Phys. Rev. Lett.* **2010**, *105* (25), 257601.

(10) Förster, M.; Paschen, T.; Krüger, M.; Lemell, C.; Wachter, G.; Libisch, F.; Madlener, T.; Burgdörfer, J.; Hommelhoff, P. Two-Color Coherent Control of Femtosecond Above-Threshold Photoemission from a Tungsten Nanotip. *Phys. Rev. Lett.* **2016**, *117* (21), 217601.

(11) Feist, A.; Bach, N.; Rubiano da Silva, N.; Danz, T.; Möller, M.; Priebe, K. E.; Domröse, T.; Gatzmann, J. G.; Rost, S.; Schauss, J.; et al. Ultrafast transmission electron microscopy using a laser-driven field emitter: Femtosecond resolution with a high coherence electron beam. *Ultramicroscopy* **2017**, *176*, 63−73.

(12) Karkare, S.; Adhikari, G.; Schroeder, W. A.; Nangoi, J. K.; Arias, T.; Maxson, J.; Padmore, H. Ultracold Electrons via Near-Threshold Photoemission from Single-Crystal Cu(100). *Phys. Rev. Lett.* **2020**, *125* (5), 054801.

(13) Li, C.; Zhou, X.; Zhai, F.; Li, Z.; Yao, F.; Qiao, R.; Chen, K.; Cole, M. T.; Yu, D.; Sun, Z.; et al. Carbon Nanotubes as an Ultrafast Emitter with a Narrow Energy Spread at Optical Frequency. *Adv. Mater.* **2017**, *29* (30), 1701580.

(14) Durham, D. B.; Riminucci, F.; Ciabattini, F.; Mostacci, A.; Minor, A. M.; Cabrini, S.; Filippetto, D. Plasmonic Lenses for Tunable Ultrafast Electron Emitters at the Nanoscale. *Phys. Rev. Appl.* **2019**, *12* (5), 054057.

(15) Hong, C.; Zou, W.; Ran, P.; Tanaka, K.; Matzelle, M.; Chiu, W.-C.; Markiewicz, R. S.; Barbiellini, B.; Zheng, C.; Li, S.; et al. Anomalous intense coherent secondary photoemission from a perovskite oxide. *Nature* **2023**, *617* (7961), 493−498.

(16) Peng, X.; Wang, Z.; Liu, Y.; Manos, D. M.; Poelker, M.; Stutzman, M.; Tang, B.; Zhang, S.; Zou, J. Optical-Resonance-Enhanced Photoemission from Nanostructured GaAs Photocathodes. *Phys. Rev. Appl.* **2019**, *12* (6), 064002.

(17) Parzyck, C. T.; Galdi, A.; Nangoi, J. K.; DeBenedetti, W. J. I.; Balajka, J.; Faeth, B. D.; Paik, H.; Hu, C.; Arias, T. A.; Hines, M. A.; et al. Single-Crystal Alkali Antimonide Photocathodes: High Efficiency in the Ultrathin Limit. *Phys. Rev. Lett.* **2022**, *128* (11), 114801.

(18) Li, Y.; Jiang, P.; Lyu, X.; Li, X.; Qi, H.; Tang, J.; Xue, Z.; Yang, H.; Lu, G.; Sun, Q.; et al. Revealing low-loss dielectric near-field modes of hexagonal boron nitride by photoemission electron microscopy. *Nat. Commun.* **2023**, *14* (1), 4837.

(19) Cassabois, G.; Valvin, P.; Gil, B. Hexagonal boron nitride is an indirect bandgap semiconductor. *Nat. Photonics* **2016**, *10* (4), 262−266.

(20) Rah, Y.; Jin, Y.; Kim, S.; Yu, K. Optical analysis of the refractive index and birefringence of hexagonal boron nitride from the visible to near-infrared. *Opt. Lett.* **2019**, *44* (15), 3797−3800.

(21) Lee, S.-Y.; Jeong, T.-Y.; Jung, S.; Yee, K.-J. Refractive Index Dispersion of Hexagonal Boron Nitride in the Visible and Near-Infrared. *Phys. Status Solidi B* **2019**, *256* (6), 1800417.

(22) Chaves, A.; Azadani, J. G.; Alsalman, H.; da Costa, D. R.; Frisenda, R.; Chaves, A. J.; Song, S. H.; Kim, Y. D.; He, D.; Zhou, J.; et al. Bandgap engineering of two-dimensional semiconductor materials. *npj 2D Mater. Appl.* **2020**, *4* (1), 29.

(23) Li, Y.; Chernikov, A.; Zhang, X.; Rigosi, A.; Hill, H. M.; van der Zande, A. M.; Chenet, D. A.; Shih, E.-M.; Hone, J.; Heinz, T. F. Measurement of the optical dielectric function of monolayer transition-metal dichalcogenides: MoS_2, $MoSe_2$, WS_2, and WSe_2. *Phys. Rev. B* **2014**, *90* (20), 205422.

(24) Carvalho, A.; Ribeiro, R. M.; Castro Neto, A. H. Band nesting and the optical response of two-dimensional semiconducting transition metal dichalcogenides. *Phys. Rev. B* **2013**, *88* (11), 115205.

(25) Montblanch, A. R. P.; Barbone, M.; Aharonovich, I.; Atatüre, M.; Ferrari, A. C. Layered materials as a platform for quantum technologies. *Nat. Nanotechnol.* **2023**, *18* (6), 555−571.

(26) Caldwell, J. D.; Aharonovich, I.; Cassabois, G.; Edgar, J. H.; Gil, B.; Basov, D. N. Photonics with hexagonal boron nitride. *Nat. Rev. Mater.* **2019**, *4* (8), 552−567.

(27) Kang, J.; Tongay, S.; Zhou, J.; Li, J.; Wu, J. Band offsets and heterostructures of two-dimensional semiconductors. *Appl. Phys. Lett.* **2013**, *102* (1), 012111.

(28) Ogawa, S.; Yamada, T.; Kadowaki, R.; Taniguchi, T.; Abukawa, T.; Takakuwa, Y. Band alignment determination of bulk h-BN and graphene/h-BN laminates using photoelectron emission microscopy. *J. Appl. Phys.* **2019**, *125* (14), 144303.

(29) Pierucci, D.; Zribi, J.; Henck, H.; Chaste, J.; Silly, M. G.; Bertran, F.; Le Fevre, P.; Gil, B.; Summerfield, A.; Beton, P. H.; et al. Van der Waals epitaxy of two-dimensional single-layer h-BN on graphite by molecular beam epitaxy: Electronic properties and band structure. *Appl. Phys. Lett.* **2018**, *112* (25), 253102.

(30) Tawfik, S. A.; Ali, S.; Fronzi, M.; Kianinia, M.; Tran, T. T.; Stampfl, C.; Aharonovich, I.; Toth, M.; Ford, M. J. First-principles investigation of quantum emission from hBN defects. *Nanoscale* **2017**, *9* (36), 13575−13582.

(31) Jungwirth, N. R.; Fuchs, G. D. Optical Absorption and Emission Mechanisms of Single Defects in Hexagonal Boron Nitride. *Phys. Rev. Lett.* **2017**, *119* (5), 057401.

(32) Libbi, F.; de Melo, P. M. M. C.; Zanolli, Z.; Verstraete, M. J.; Marzari, N. Phonon-Assisted Luminescence in Defect Centers from Many-Body Perturbation Theory. *Phys. Rev. Lett.* **2022**, *128* (16), 167401.

(33) Reimers, J. R.; Shen, J.; Kianinia, M.; Bradac, C.; Aharonovich, I.; Ford, M. J.; Piecuch, P. Photoluminescence, photophysics, and photochemistry of the V_B^- defect in hexagonal boron nitride. *Phys. Rev. B* **2020**, *102* (14), 144105.

(34) Tran, T. T.; Bray, K.; Ford, M. J.; Toth, M.; Aharonovich, I. Quantum emission from hexagonal boron nitride monolayers. *Nat. Nanotechnol.* **2016**, *11* (1), 37−41.

(35) Hou, S.; Birowosuto, M. D.; Umar, S.; Anicet, M. A.; Tay, R. Y.; Coquet, P.; Tay, B. K.; Wang, H.; Teo, E. H. T. Localized emission from laser-irradiated defects in 2D hexagonal boron nitride. *2D Mater.* **2017**, *5* (1), 015010.

(36) Gao, X.; Pandey, S.; Kianinia, M.; Ahn, J.; Ju, P.; Aharonovich, I.; Shivaram, N.; Li, T. Femtosecond Laser Writing of Spin Defects in Hexagonal Boron Nitride. *ACS Photonics* **2021**, *8* (4), 994−1000.

(37) Chow, P. K.; Jacobs-Gedrim, R. B.; Gao, J.; Lu, T.-M.; Yu, B.; Terrones, H.; Koratkar, N. Defect-Induced Photoluminescence in Monolayer Semiconducting Transition Metal Dichalcogenides. *ACS Nano* **2015**, *9* (2), 1520−1527.

(38) Shi, W.; Lin, M.-L.; Tan, Q.-H.; Qiao, X.-F.; Zhang, J.; Tan, P.-H. Raman and photoluminescence spectra of two-dimensional nanocrystallites of monolayer WS_2 and WSe_2. *2D Mater.* **2016**, *3* (2), 025016.

(39) Li, Y.; Liu, W.; Wang, Y.; Xue, Z.; Leng, Y.-C.; Hu, A.; Yang, H.; Tan, P.-H.; Liu, Y.; Misawa, H.; et al. Ultrafast Electron Cooling and Decay in Monolayer WS2 Revealed by Time- and Energy-Resolved Photoemission Electron Microscopy. *Nano Lett.* **2020**, *20* (5), 3747−3753.

(40) Chee, S.-S.; Lee, W.-J.; Jo, Y.-R.; Cho, M. K.; Chun, D.; Baik, H.; Kim, B.-J.; Yoon, M.-H.; Lee, K.; Ham, M.-H. Atomic Vacancy Control and Elemental Substitution in a Monolayer Molybdenum Disulfide for High Performance Optoelectronic Device Arrays. *Adv. Funct. Mater.* **2020**, *30* (11), 1908147.

(41) Wang, Y.; Xie, Y.; Dai, Y.; Han, X.; Huang, Y.; Gao, Y. Intensive and broad bound exciton emission at cryogenic temperature in suspended monolayer transition metal dichalcogenides. *Phys. Rev. Mater.* **2022**, *6* (11), L111001.

(42) Carozo, V.; Wang, Y.; Fujisawa, K.; Carvalho, B. R.; McCreary, A.; Feng, S.; Lin, Z.; Zhou, C.; Perea-López, N.; Elías, A. L.; et al. Optical identification of sulfur vacancies: Bound excitons at the edges of monolayer tungsten disulfide. *Sci. Adv.* **2017**, *3* (4), No. e1602813.

(43) Wang, H.; Zhang, C.; Rana, F. Ultrafast Dynamics of Defect-Assisted Electron-Hole Recombination in Monolayer MoS_2. *Nano Lett.* **2015**, *15* (1), 339−345.

(44) Li, L.; Lin, M.-F.; Zhang, X.; Britz, A.; Krishnamoorthy, A.; Ma, R.; Kalia, R. K.; Nakano, A.; Vashishta, P.; Ajayan, P.; et al. Phonon-Suppressed Auger Scattering of Charge Carriers in Defective Two-Dimensional Transition Metal Dichalcogenides. *Nano Lett.* **2019**, *19* (9), 6078−6086.

(45) Gottscholl, A.; Kianinia, M.; Soltamov, V.; Orlinskii, S.; Mamin, G.; Bradac, C.; Kasper, C.; Krambrock, K.; Sperlich, A.; Toth, M.; et al. Initialization and read-out of intrinsic spin defects in a van der Waals crystal at room temperature. *Nat. Mater.* **2020**, *19* (5), 540−545.

(46) Gu, R.; Wang, L.; Zhu, H.; Han, S.; Bai, Y.; Zhang, X.; Li, B.; Qin, C.; Liu, J.; Guo, G.; et al. Engineering and Microscopic Mechanism of Quantum Emitters Induced by Heavy Ions in hBN. *ACS Photonics* **2021**, *8* (10), 2912−2922.

https://doi.org/10.1021/acs.jpcc.3c07843
J. Phys. Chem. C 2024, 128, 4286−4294